

Achieving Dual-Function In Situ Monitoring of Water Level and Flow Velocity via a Flapping-Wing Triboelectric Nanogenerator

Xinxian Wang, Hengyu Li, Jiacheng Zhang, Siyang He, Jianlong Wang, Yanrui Zhao, Xin Guo, Yang Yu,* Zhong Lin Wang,* and Tinghai Cheng*

Real-time monitoring of water level and flow velocity is essential for reflecting hydrodynamic properties, serving as a core component of intelligent hydrological monitoring systems. However, the measurement accuracy and anti-interference capabilities of existing sensing methods limit their practical applications. Here, a flapping-wing water level-velocity method (FWVM) is proposed, which combines the flapping-wing motion with the triboelectric nanogenerator (TENG). Through the decoupling analysis of the TENG characteristic signal reflected by the flapping wing motion, the information of water level and flow velocity is extracted. Based on this method, a self-sustaining flapping wing TENG (FW-TENG) with a water level resolution of 1 mm is established. The accuracy and stability of FW-TENG are improved through optimization of the wing shape and the magnetic drive design. Furthermore, a dual-function monitoring system has been developed for real-time in situ monitoring and early warning of water level and flow velocity. Compared with a commercial sensor, the error rates of maximum water level and flow velocity are below 0.45% and 2%, respectively. This research provides an approach for the development of underwater sensors and holds great potential for widespread application in hydrological monitoring.

Water level and flow velocity are two key parameters in hydrological monitoring, providing basic data and a scientific basis for a comprehensive understanding of hydrological processes.^[1,2] Currently, various methods are employed to monitor water level and flow velocity, including traditional manual observation of contact, radar, acoustic, and image methods.^[3–5] Despite significant advances in monitoring technologies, water level and flow velocity sensors still face challenges such as response time, reliability, and environmental constraints. For example, the traditional artificial observation method is easy to be affected by human error, resulting in low measurement accuracy, poor real-time performance, and other issues.^[6,7] Radar method, acoustic method, and image method in water level and flow velocity monitoring have adopted advanced technical means. However, in real water environments, environmental factors such as electromagnetic interference, temperature, and humidity can significantly

affect the accuracy.^[8] Furthermore, the water level and the flow velocity monitored by the system are relatively independent, and the acquisition and processing of the flow velocity measurements are often treated independently, with separate circuits and algorithms required for data acquisition and processing, which adds to system complexity.^[9,10] Therefore, developing an integrated and highly robust sensing technology for water level and velocity is essential.

In 2012, Zhong Lin Wang's team first proposed the triboelectric nanogenerator (TENG).^[11] Due to the advantages of TENG, such as high sensitivity and short response time,^[12–15] self-powered sensing technology has been widely used in medical health,^[16] industrial monitoring,^[17,18] environmental monitoring,^[19–23] artificial intelligence^[24] and other fields. In environmental monitoring, various sensor technologies based on the TENG principle have been proposed, such as flow monitoring for the pipeline environment,^[25,26] wind speed monitoring for the wind environment^[27,28] and rainfall monitoring for the rainfall environment.^[29,30] These studies indicate that TENG sensor technology offers significant advantages, such as strong anti-environmental interference ability and the ability without an external power supply, which can well avoid the impact of

1. Introduction

Hydrological monitoring plays a crucial role in water resources management, flood early warning, and ecological protection.

X. Wang, H. Li, J. Zhang, S. He, J. Wang, Y. Zhao, X. Guo, Y. Yu, Z. L. Wang, T. Cheng
Beijing Institute of Nanoenergy and Nanosystems
Chinese Academy of Sciences
Beijing 101400, P. R. China
E-mail: yuyang@binn.cas.cn; zhong.wang@mse.gatech.edu; chengtinghai@binn.cas.cn

X. Wang, H. Li, S. He, J. Wang, Y. Zhao, X. Guo, Y. Yu, T. Cheng
School of Nanoscience and Engineering
University of Chinese Academy of Sciences
Beijing 100049, P. R. China
Z. L. Wang, T. Cheng
Guangzhou Institute of Blue Energy
Guangzhou 510555, P. R. China

The ORCID identification number(s) for the author(s) of this article can be found under <https://doi.org/10.1002/adfm.202506045>

DOI: 10.1002/adfm.202506045

interference caused by environmental factors such as electromagnetic and temperature on sensing accuracy. However, hydrological monitoring technology in river and open channel environments remains underexplored, particularly in the monitoring of water level and flow velocity. The complexity of river and open-channel environments, coupled with the uneven distribution of flow velocity across cross-sections, makes current multi-point velocity measurement techniques difficult to express the true velocity distribution of the cross-section.

Additionally, current water level and flow velocity sensors usually have independent structures, resulting in cumbersome data acquisition, processing, and analysis processes and low system integration, which cannot meet the demand for real-time monitoring and efficient integration.^[31–34] Therefore, it is urgent to develop a new monitoring technique that not only improves system integration but also accurately characterizes flow velocity and water level changes in complex environments. The combination of flapping wing structure and TENG technology is a powerful solution to this challenge. In river and open-channel environments, flow velocity varies at different water levels across the cross-section.^[35–37] The flapping wing structure can sense the change of flow velocity through its unique dynamic characteristics, and convert this physical change into electrical signals through TENG technology, thus realizing real-time synchronous monitoring of water level and flow velocity. Furthermore, this innovative approach not only improves system integration and robustness, but also significantly reduces external disturbances, improves monitoring accuracy, and improves overall system performance.

In this work, a method for real-time in situ monitoring of water level and flow velocity by integrating flapping wing motion with TENG technology is proposed. Combined with the motion mechanism of the flapping wing, the signal generated by TENG can decouple and analyze the flapping wing motion to achieve the simultaneous monitoring of water level and flow velocity. The surface pressure coefficients, lift, and flapping stability of various flapping-wing shapes are analyzed through fluid simulation calculations, which proves that the NACA 0015 flapping wing exhibits excellent starting performance and motion stability in water flow. At the same time, the transmission accuracy is improved by optimizing the design of the magnetic drive, ensuring that the motion of the flapping wing can be transmitted to TENG unit accurately. Subsequently, a self-powered flapping wing triboelectric nanogenerator (FW-TENG) is designed for water level and flow velocity monitoring. The static characteristics of FW-TENG, including linearity, repeatability, and hysteresis, are investigated by setting up a test system simulating a real water flow environment. Finally, an integrated monitoring and early warning system is developed, enabling dual-function in situ monitoring. When the water level and flow velocity exceed the warning value, real-time alerts are triggered. Compared to commercial Doppler sensors, the FW-TENG demonstrates a maximum water level error rate of less than 0.45% under varying water level conditions and a maximum flow velocity error rate of less than 2% under different flow velocity conditions. This research holds great promise for advancing the application of TENG sensing technology in the field of hydrological monitoring.

2. Results and Discussion

2.1. Method for Water Level and Flow Velocity Monitoring

With the aggravation of global climate change and the influence of human activities, the abnormal changes of river water level and flow velocity are becoming more frequent, which has a profound impact on agricultural irrigation, urban water supply, and hydropower generation.^[38,39] Currently, hydrological monitoring stations are used to monitor the water level and flow velocity of rivers and open channels, providing key parameters for hydrological forecasting models and providing a scientific basis for disaster warnings, as shown in **Figure 1a**. Although traditional monitoring methods play an important role in monitoring the water level and velocity of rivers and open channels to some extent, there are still many problems and deficiencies in practical application. There are two main challenges, as shown in **Figure 1b**. In rivers and open channels, the accuracy and stability of sensors are usually affected by environmental factors such as bubbles, electromagnetism, temperature, and humidity, and there are often data errors and drift phenomena that affect the accuracy and credibility of monitoring data. In addition, most of the velocity monitored by current sensors is the surface velocity of water or the velocity measured by the multi-point method. The velocity on the surface of the water body is usually significantly different from that in the water body. Because of bed friction, fluid layer interaction, and water structure, surface velocity is higher than deep velocity.^[40] Such differences can lead to biased estimates of actual flow velocities. Multi-point velocity measurement is a method to obtain velocity distribution by setting multiple measurement points at different depths and positions of the water body.^[41,42] However, the selection and distribution of measurement points may not fully represent the velocity distribution characteristics of the dynamic water body. Therefore, it is difficult to accurately measure the true velocity of the water body section by traditional measurement methods.

Based on the above problems, a method combining TENG and flapping wings is proposed to monitor water level and flow velocity. The specific working principle of this method is mainly divided into four stages, and the corresponding TENG signal is generated, as shown in **Figure 1c**. The limiting position I float on the water surface and can change with the change of water level. The limiting position II is fixed under the water, and the flapping wing continuously moves between the two limiting positions, and the flapping wing can only move linearly and rotate in the vertical flow direction by limiting the freedom degree of the flapping wing, and all the movements are directly generated by fluid force. The continuous flapping motion of the flapping wing in water flow consists of two stages: the pure heave stage (rise and fall phase) and the stroke reversal stage (pitch phase). When the water flow passes by the flapping wing, the fluid separates on the surface of the flapping wing and forms a vortex. Due to the existence of a certain pitch angle of the flapping wing, the pressure difference between the upper and lower surfaces causes the flapping wing to move up and down (rise and fall phase), thus transmitting the motion to the sensing unit by driving the magnetic drive part to generate the output signal, as shown in **Figure 1c(i,iii)**. No electrical signals are generated during the pitch phase (**Figure 1c(ii,iv)**). By analyzing the pulse number of

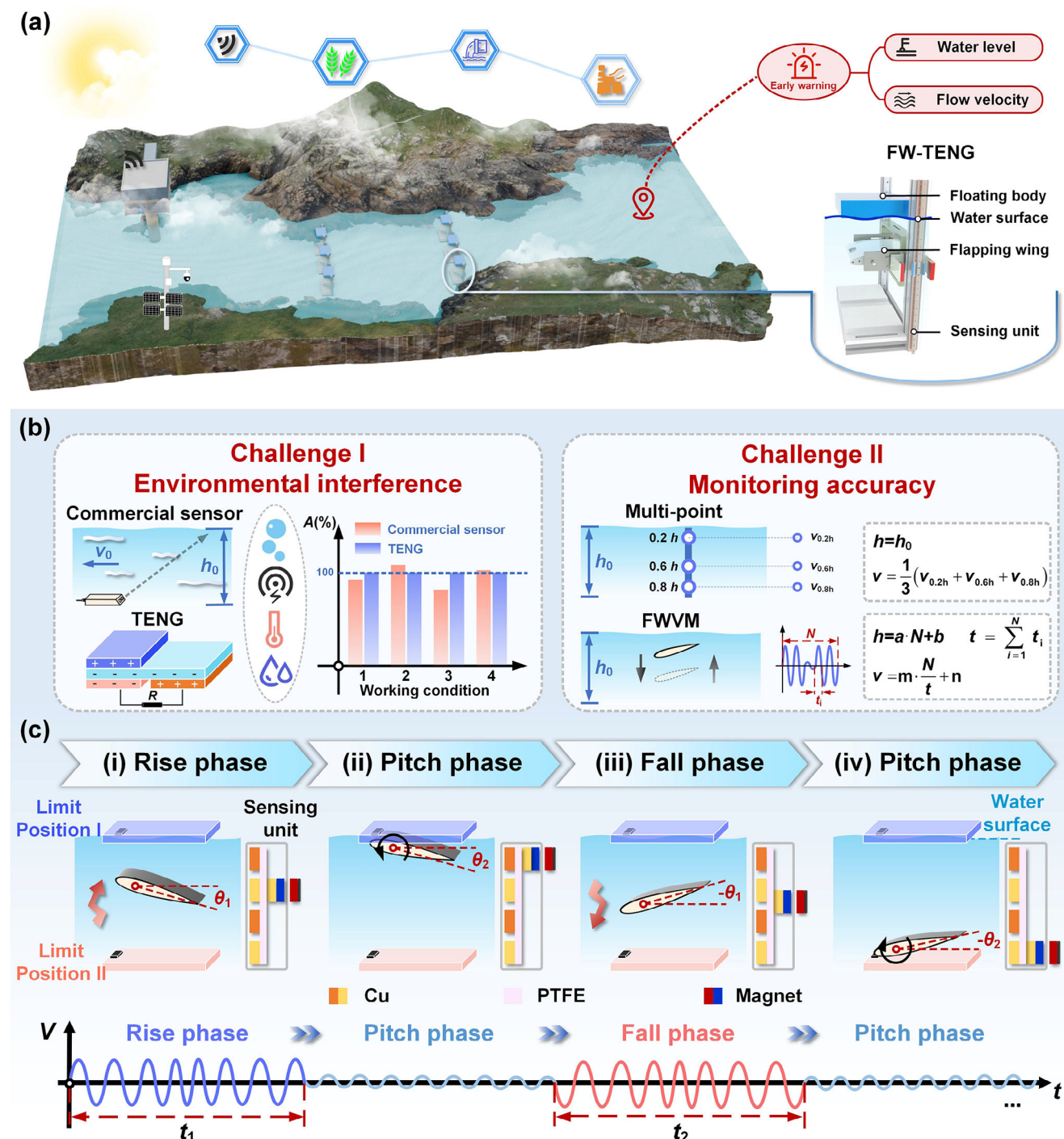


Figure 1. Implementation process of flapping-wing water level-flow velocity method: a) Application scenario; b) Detailed analysis of FWVM; c) Working principle diagram of monitoring flow velocity and water level.

the electrical signal in the rise and fall phases, the real water level change is analyzed. The flow velocity will affect the velocity of the flapping wing. This motion-signal mapping relationship realizes the physical decoupling of flapping motion and then uses signal processing technology to decouple and analyze the corresponding motion stage signals to achieve in situ monitoring of water level and flow velocity.

Based on the above physical mechanism, a strict mathematical characterization model is established.

Water level monitoring: Based on the pulse number (N) at heave stages (rise or fall), a quantitative correlation model of flapping wing displacement is constructed:

$$L_x = aN \quad (1)$$

where L_x denotes the flapping displacement and a denotes the displacement resolution. Given that the limit position I (floating body) maintains a fixed draft (c), a quantitative relationship for water level (h) can be derived as follows:

$$h = L_x + c \quad (2)$$

Flow velocity monitoring: At a constant water level, experimental tests with varying flow velocities are conducted. Through analysis of time-frequency features in the rise or fall phase pulse signals, a linear correlation between flow velocity (v) and mean flapping velocity (v_m) is established:

$$v_m = \frac{aN}{t} \quad (3)$$

$$v = mv_m + n \quad (4)$$

where m and n are the slope and intercept in the linear relationship. According to the above test process, flow velocity experiments are carried out under different water levels to obtain multiple m and n , and the quantitative relationship between water level, m and n is constructed, and then the 3D mapping relationship between flow velocity, mean flow velocity, and water level is obtained. In summary, this study successfully achieved the decoupled monitoring of water level and flow velocity through the dynamic separation of flapping motion, feature extraction of TENG signals, and mathematical modeling.

2.2. Flapping Wing Motion and Simulation Analysis

In order to accurately describe the motion of the flapping wing, the force on the wing structure underwater flow conditions is analyzed first. Take NACA 0015 as an example, as shown in **Figure 2a(i)**, where the x -axis is parallel to the chord line and the y -axis is perpendicular to the chord line. NACA 0015 flapping wing in the impact of the water flow, lift (F_{wy}) and chord perpendicular, drag (F_{wx}), and chord parallel. The lift coefficient C_{Fwy} and torque coefficients C_M are defined as follows:^[43]

$$C_{Fwy} = \frac{2F_{wy}}{\rho U^2 CS} \quad (5)$$

$$C_M = \frac{2M}{\rho U^2 CS} \quad (6)$$

where the fluid density of ρ , the flow velocity of U , the chord length of C , the span of S , and the pitch torque loaded on the wing of M . When the water flow impacts the flapping wing, due to the existence of the pitch limiter, the flapping wing can realize continuous flapping in the water flow, and the flapping wing will present different states. **Figure 2a(ii)** shows the pressure distribution on the surface of the flapping wing in three main states (positive and negative pressures generated on the wing surface). It is worth noting that the pressure (positive and negative) on the flapping wing surface can generate lift, which drives the flapping wing up and down. The two stages of flapping wing motion in water flow are analyzed in detail, where D is the flapping distance, x_p is the distance from the pivot point to the flapping wing leading

edge, and the pitch angle (θ) is constant at 30° during pure heave phase, as shown in **Figure S1** (Supporting Information). During the stroke reversal phase, the limiter contacts the leading edge of the flapping wing, forcing the flapping wing to rotate, changing its pitch angle, and the flapping wing remains rotated until it contacts another pitch limiter to begin the next pure heave phase, as shown in **Figure S1b,d** (Supporting Information). In order to verify the accuracy of the above analysis, a transient numerical simulation of the hydrodynamic performance of 2D flapping wing system is carried out by using dynamic mesh technology in combination with the user-defined function (UDF) of commercial finite element software ANSYS FLUENT. The calculation domain and mesh generation structure are shown in **Figure S2** (Supporting Information). The selected simulation object is a NACA 0015 flapping wing with a chord length C of 20 cm, and its pitch axis is located at $1/3 C$ relative to the leading edge of the flapping wing. In addition, the boundary condition of the flapping wing surface is set as the wall boundary. The left boundary is the velocity inlet, the right boundary is the pressure outlet, and the upper and lower boundaries are provided with wall boundaries. Water flows from the velocity inlet to the pressure outlet, driving the flapping wing to move continuously. **Figure 2b** shows the pressure distribution of NACA 0015 at different stages of a cycle. It is worth noting that vortices existing at the leading edge of the flapping wing are pushed up (down) by the upward (down) moving flapping wing and remain near the flapping wing, forming a low-pressure region near the leading edge of the flapping wing, thereby enhancing lift and pitch moment. The pitch rotation of the flapping wing occurs at the top of the rise phase and at the bottom of the fall phase, where the pitch angle of motion is constant. The simulated motion characteristics are consistent with the analysis of **Figure S2** (Supporting Information) above.

In fully passive motion, the up-down motion and pitch motion are derived entirely by fluid-structure interaction. The water flow generates forces on the flapping wing, causing it to flutter up and down, and the motion of the flapping wing in turn, changes the generation of forces. Therefore, the flapping wing is the part that directly interacts with the water flow, the dynamic performance of different flapping wings under the water flow condition is different, and the shape of the flapping wing is the key factor affecting the stability of motion. In order to evaluate the dynamic performance of different flapping wing shapes, simulation analysis of four different flapping wing shapes (triangle wing, rectangular wing, elliptical wing, and rhombus wing with chord length C) is carried out under the same flow conditions. The flapping frequency, the pressure difference between the upper and lower surfaces, and the flapping stability of the flapping wing are studied emphatically. According to the vorticity and surface pressure distribution around the flapping wing, the motion characteristics are analyzed, and the results are shown in **Movie S1** (Supporting Information). **Figure 2c** shows flapping frequencies for five different flapping wings under the same flow conditions. The results show that the flapping frequency of NACA 0015 is faster, which indicates that the wing is subjected to greater lift and has better start-up performance. **Figure 2d** shows the pressure coefficient curves of five kinds of flapping wings, in which the pressure coefficient envelope area can reflect the lift coefficient of the flapping wing. The area enclosed by the pressure coefficient of NACA 0015 is the largest, so the lift coefficient of the NACA 0015 at this

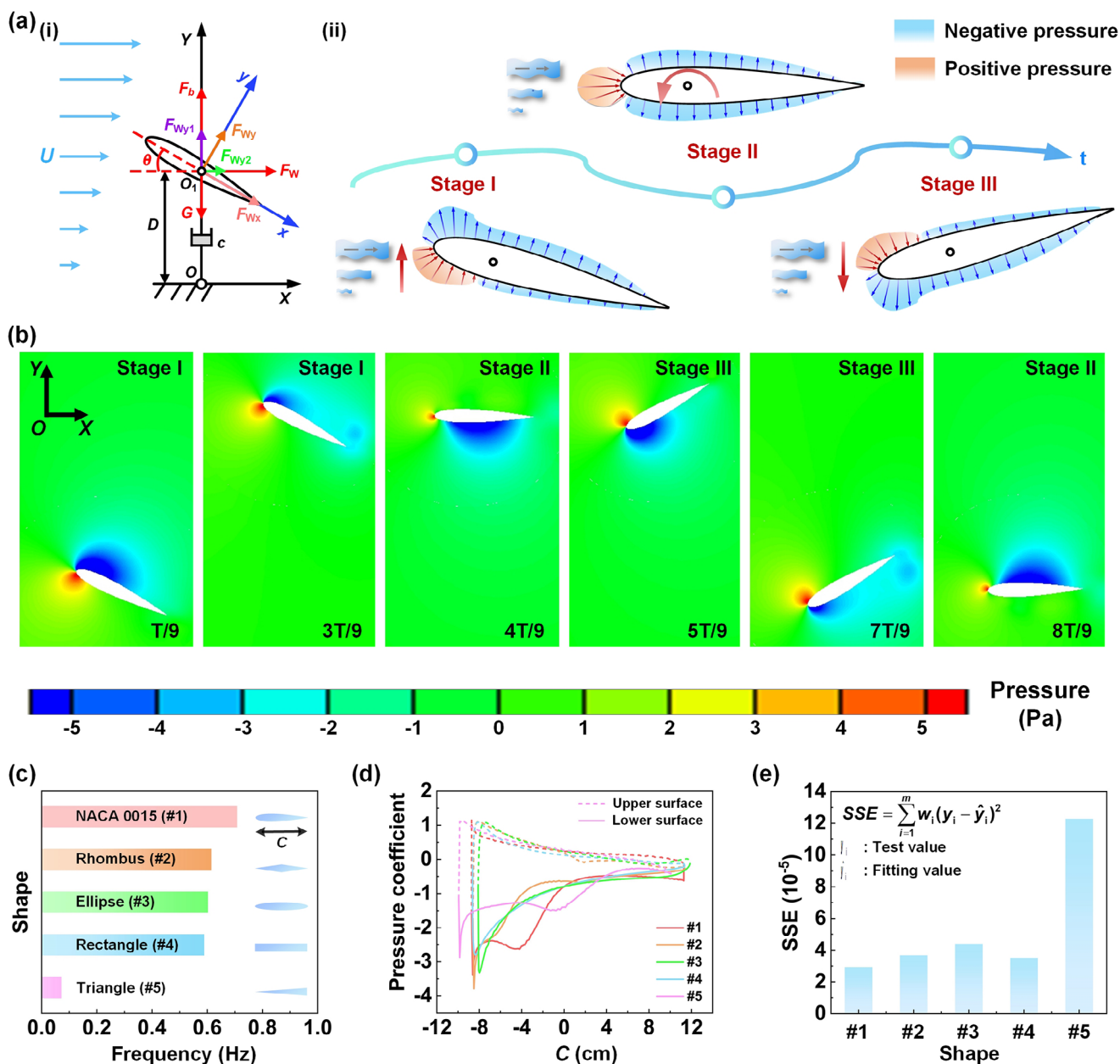


Figure 2. Flapping wing motion and simulation analysis: a) Force analysis of flapping wing in water flow; b) Pressure distribution of NACA 0015; c) Flapping frequency under different airfoils; d) Pressure coefficient curves of different airfoils; e) The sum variance of the acceleration of different airfoils compared with their corresponding uniform acceleration.

angle of attack is the largest and the stability is the best. In addition, the acceleration change of the flapping wing will directly affect the dynamic stability of the flapping wing motion. Frequent changes in acceleration will make the flapping wing subject to more complex dynamic hydrodynamic loads, which may lead to a more complex dynamic response of the flapping wing system and increase instability factors. At the same time, it may also cause the disorder of the flow field, further affect the lift of the flapping wing, and reduce the flapping stability. Therefore, as shown in Figure 2e, the acceleration changes under different airfoils and their corresponding uniform acceleration are compared and an-

alyzed. The results show that the sum variance of NACA 0015 is the smallest, and the smaller the sum variance, the better the dynamic stability. Therefore, NACA 0015 is selected as the flapping wing used in the study.

2.3. Basic Performance Test of the TENG Unit

According to the movement form of the flapping wing, a motor test platform is built, which is mainly composed of a motor, a slider, a connecting module, and TENG unit, as shown in

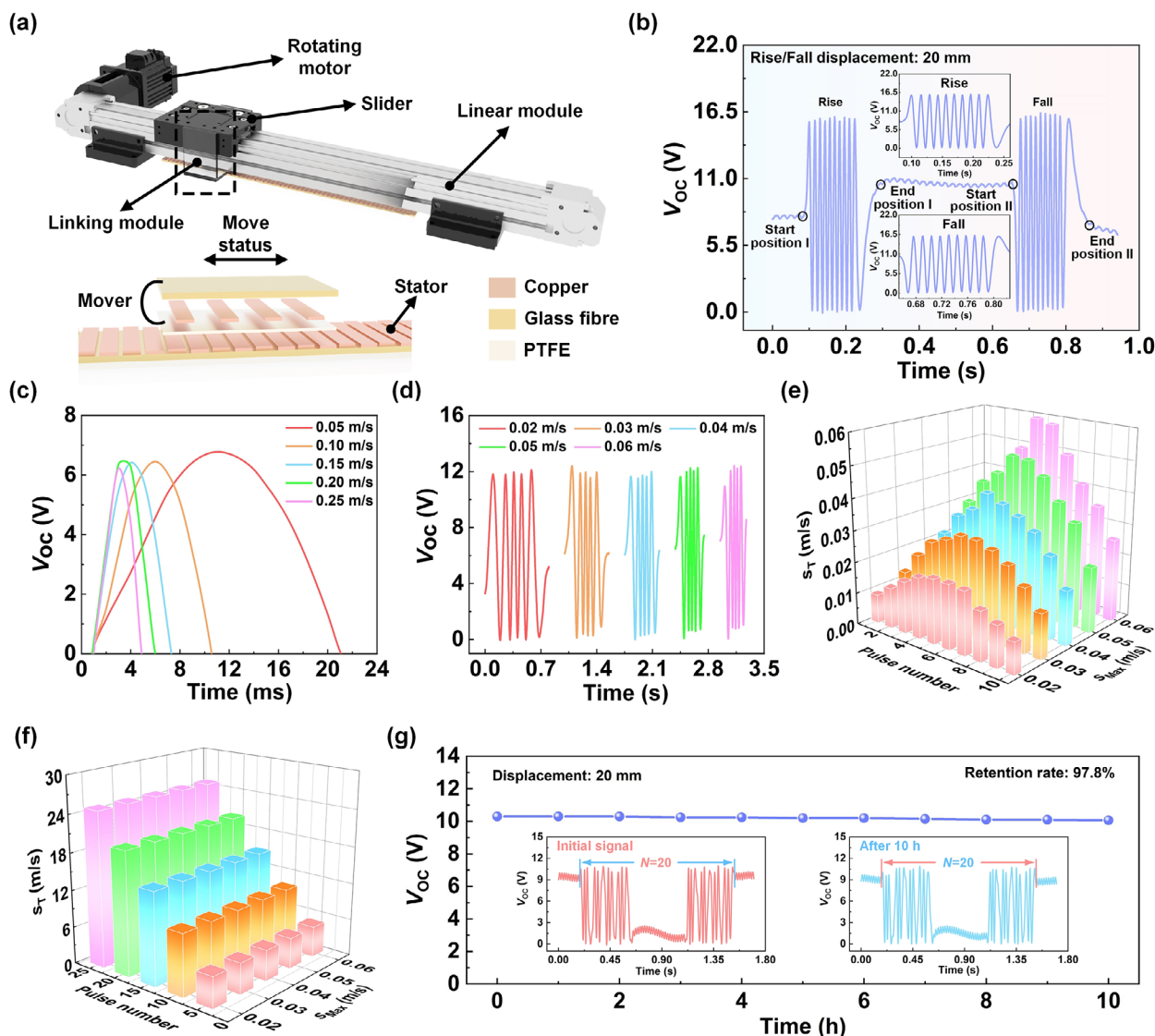


Figure 3. Basic performance test of the TENG unit: a) Schematic diagram of motor test system; b) The open-circuit voltage of the flapping wing under a cycle; c) The open-circuit voltage with a displacement of 1 mm at different speeds; d) The open-circuit voltage under different accelerated motion; e) At a displacement of 10 mm, the speed of each displacement of 1 mm under different accelerated motion; f) The number of pulses with different displacements under different acceleration motions; g) Durability of the TENG unit.

Figure 3a. The width and spacing of the electrodes on the stator and rotor of the TENG unit are uniform (Figure S3a, Supporting Information), copper is used as electrode material, and Polytetrafluoroethylene (PTFE) as friction material. As shown in Figure S3b (Supporting Information), due to the polarity difference between the two materials in contact on the mover and stator, electrode II on the mover is positively charged, while the PTFE film covering electrode I on the stator is negatively charged by an equal amount. When the electrodes on the mover are aligned with the electrodes in the interleaved electrode pairs on the stator, there is no charge transfer between the interleaved electrode pairs on the stator due to electrostatic equilibrium. As the mover moves forward, the electrostatic balance is broken, causing electrons to flow from left to right on the interleaved electrode pairs on the stator, forming a new equilibrium state.

Therefore, when electrode II alternately contacts the electrodes of the interleaved electrode pairs, a continuous alternating current signal will be generated. As shown in Figure S3c (Supporting Information), the open-circuit potential distribution under the above process is simulated by COMSOL Multiphysics. The results are consistent with those described in Figure S3b (Supporting Information). Resolution is the minimum detectable displacement, which is determined by the electrode width and spacing of the TENG unit. The displacement resolution designed in this paper is 1 mm, which means that every 1 mm displacement of the mover produces a pulse signal. By counting the number of pulse signals, the actual displacement of the mover can be determined.

According to the flapping wing motion mechanism analyzed in Figure 2b, the reciprocating linear motion of the flapping wing

is simulated by using a motor, and the mover on the linkage module is driven to move so that the mover slides linearly on the stator of the TENG unit to generate an electrical signal. Therefore, as shown in Figure 3b, the output signal generated by its motion under one cycle is simulated by the motor, where start position I to end position I and start position II to end position II are the pure-heaving phase (rise and fall phase), and end position I to start position II is a stroke-reversal phase (pitch phase). The mover is fixed on the linking module of the linear motor, and the stator is fixed on the optical platform and in contact with the mover. In addition, by changing the speed of the motor, the output signal of the displacement of 1 mm at different speeds (0.05, 0.10, 0.15, 0.20, and 0.25 m s⁻¹) is analyzed, as shown in Figure 3c. The experimental results show that the speed information corresponding to the output signal is consistent with the speed of the motor at different speeds. Further, under the condition of constant speed, the output signals under different motor displacement conditions are analyzed, as shown in Figure S4 (Supporting Information). It is worth noting that the displacement information corresponding to the output signal is consistent with the displacement of the motor, proving that the resolution of the displacement is 1 mm, which determines the minimum displacement that can be detected. In addition, considering that the flapping wing is not a uniform motion under the impact of water flow, different acceleration motions are simulated by the motor, in which the motion form is first accelerated from 0 to the set value and then decelerated to 0. The test results show that the output signal is shown in Figure 3e under the same displacement. As shown in Figure 3f, in the displacement of 10 mm, the corresponding speed information under each 1 mm is analyzed. It can be seen that the corresponding speed information reflected under different acceleration movements is consistent with its motor motion form, and the maximum speed value of the output signal is consistent with the set values, which are 0.02, 0.03, 0.04, 0.05, and 0.06 m s⁻¹, respectively. In addition, under the above five different acceleration conditions, the pulse number of the output signal generated under different displacement conditions is analyzed and studied, and the results are consistent with the displacement of the motor. The short-circuit current of TENG unit with a displacement of 10 mm under constant speed and accelerated motion of the linear motor is shown in Figure S5 (Supporting Information). In addition to monitoring displacement and speed, the durability of a device is also important. To further evaluate the durability of the TENG unit, continuous running tests of up to 10 h were conducted by reciprocating motion at a displacement distance of 20 mm. The output signal remains almost unchanged throughout the process, and the performance retention rate after 10 h is 97.8%, indicating that it can work continuously for a long time and has excellent durability, as shown in Figure 3g.

2.4. Parameter Optimization of Magnetic Drive and Output Characteristic Test

The magnetic transmission structure transfers the flapping motion to the TENG unit, and optimizing the magnet configuration (the magnet distance and magnet gap) is particularly important because it determines the reliability of long-term mea-

surements. The balanced design must achieve high sensitivity while maintaining mechanical stability to ensure stable performance under dynamic working conditions, thereby ensuring that the sensor has both high sensitivity and durability. Therefore, the influence of magnet distance (0, 1, 2, 3, 4, 5, 6, 7, and 8 mm) on the accuracy of displacement and velocity sensing is first explored, where magnets I and II are located outside and inside the TENG unit, respectively, as shown in Figure 4a–c. As shown in Figure 4a, when the displacement is 20 mm, the displacement error rate is 0 when the magnet distance is 3 mm at different speeds, that is, the displacement is consistent with the motor, and the details of the open-circuit voltage are shown in Figure S6a (Supporting Information). As shown in Figure 4b,c, when the magnet distance is 3 mm, the average speed reflected by the sensing signal is closer to its corresponding motor speed, the standard deviation is smaller, and the representative speed error rate is lower. This is because the movement of the mover is affected by various forces such as magnetic force, gravity, and friction. The different magnet distances will affect the magnetic field distribution and affect the magnetic force received by magnet II on the mover, which may lead to the deterioration of the error rate of the output signal. A reasonable magnet distance can ensure the symmetry and uniformity of the magnetic field, and reduce the sensitivity to mechanical shock and vibration during operation, thereby improving the measurement sensitivity and enhancing the robustness of the system. In addition, the influence of the magnet gap on the accuracy of displacement and velocity sensing is studied, as shown in Figure 4d–f. The experimental results show that the displacement and velocity sensing accuracy is the highest when the magnet gap is 5 mm, and the detailed diagram of the output signal with the magnet gap of 5 mm is shown in Figure S6b (Supporting Information). With the change of driving speed, the output signal also shows a corresponding linear trend. This means that the sliding speed of the motor can be accurately and timely captured and converted into the corresponding electrical signal for output. A smaller magnetic gap increases the magnetic field strength, reduces the position offset caused by shock or vibration, and improves stability and sensitivity. However, too small a gap will increase the motion interference problem between the magnet and the package shell, causing wear on the magnet surface and reducing sensitivity. Based on the above considerations, the final magnetic transmission parameters are 3 mm magnet distance and 5 mm magnet gap.

In addition, considering the environmental conditions of practical applications, in order to ensure the stability and reliability of the output signal, the effects of different temperatures and relative humidity on the output signal are systematically studied. By placing the TENG unit in a constant temperature and humidity box and controlling the temperature and humidity, the electrical signal output is detected, as shown in Figure 4g,h. The specific output signal is shown in Figure 4i and Figure S7 (Supporting Information). The experimental results show that the sensing accuracy does not change under different temperatures and relative humidity, and the attenuation of signal amplitude is less than 0.1%, which proves that the output signal is not affected by temperature and relative humidity. The main reason for this excellent effect is that the physical isolation between the underwater flapping mechanism and the TENG sensing unit is achieved by

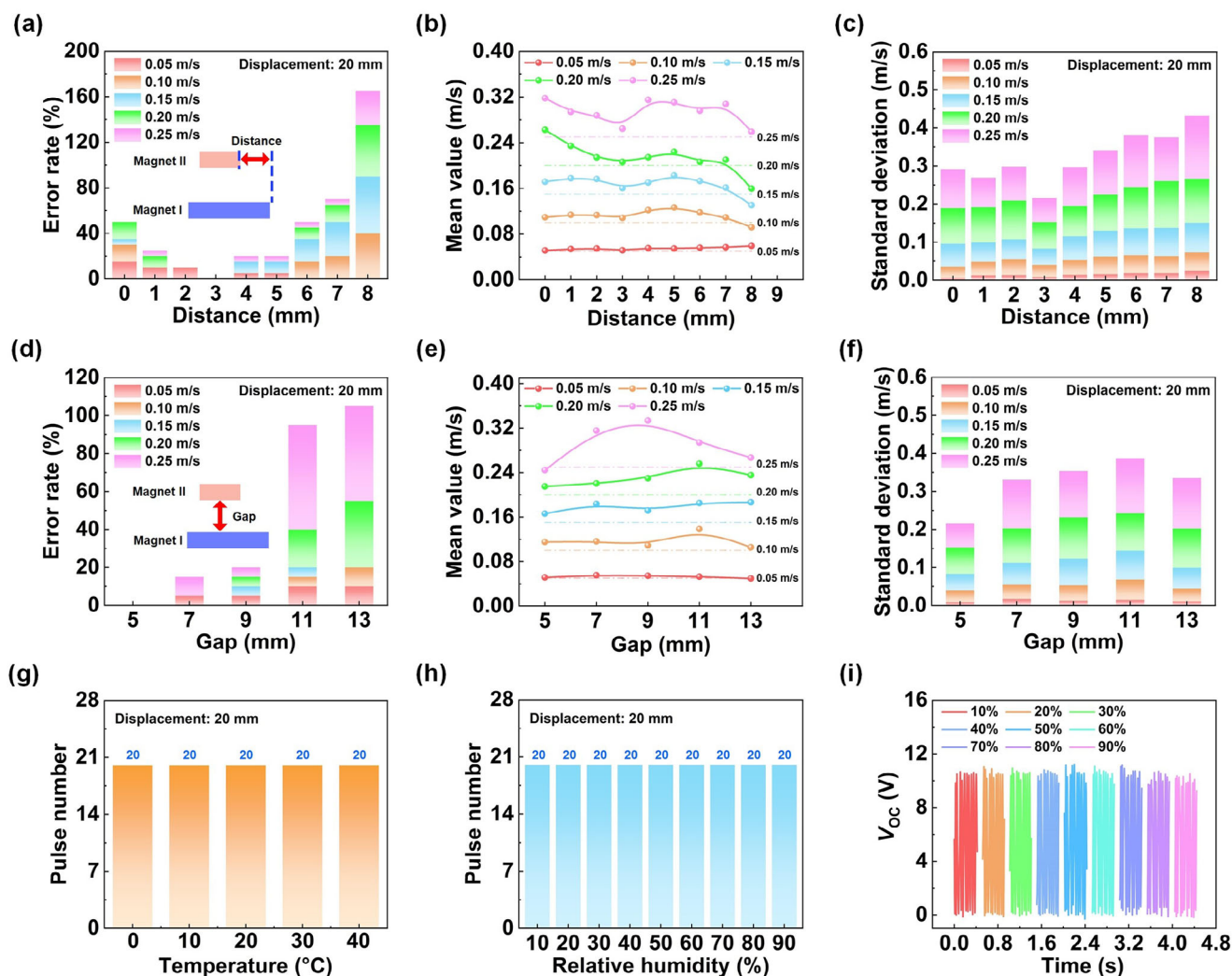


Figure 4. Parameter optimization of magnetic drive structure and output characteristics of the TENG unit: a–c) The influence of magnet distance on displacement and velocity sensing accuracy; d–f) The influence of magnetic transmission gap on the accuracy of displacement and velocity sensing; g) The influence of different temperatures on the output signal; h) The influence of different relative humidity on the output signal; i) The open-circuit voltage of different relative humidity.

establishing a non-contact magnetic transmission system. In addition, the TENG sensing unit is encapsulated as a whole using modified epoxy resin. This sealing system effectively blocks external water vapor penetration, ensuring excellent sensing performance and operational stability even in high-humidity water environments, thereby ensuring the long-term reliability of the integrated system.

2.5. Testing of the FW-TENG Sensing Characteristics

In order to verify the effectiveness of this method in monitoring water level and velocity in a real flow environment, a flapping-wing TENG is designed. The specific structure of FW-TENG is shown in Figure 5a, which mainly includes NACA 0015 flapping wing, magnetic drive modules, and TENG unit. A photograph of the prototype FW-TENG device is shown in Figure S8 (Supporting Information). Water flow passes through the NACA 0015

flapping wing, and the magnetic drive module fixed on the flapping wing moves up and down, driving the mover with magnet II to move synchronously on the stator of the TENG unit, effectively avoiding the influence of water on the TENG unit. The motion phase analysis of FW-TENG is shown in Movie S2 (Supporting Information). In order to explore the sensing characteristics of FW-TENG, FW-TENG is tested several times under different flow velocities and water levels. As shown in Figure 5b, the experimental results show that the error rate at the same water level is relatively small at different flow velocities, less than 2%. Under the condition of 0.72 m s^{-1} flow velocity, the error rate at different water levels is less than 2%, which has good water-level sensing accuracy. As shown in Figure 5c, the hysteresis characteristics were analyzed, i.e., there is a difference between the pulse number extracted from the forward and the reverse directions for the same flow velocity, and the difference after subtraction is ΔH_1 . This phenomenon is called the hysteresis characteristic, and the maximum hysteresis error rate of FW-TENG is $\approx 1.8\%$. The friction

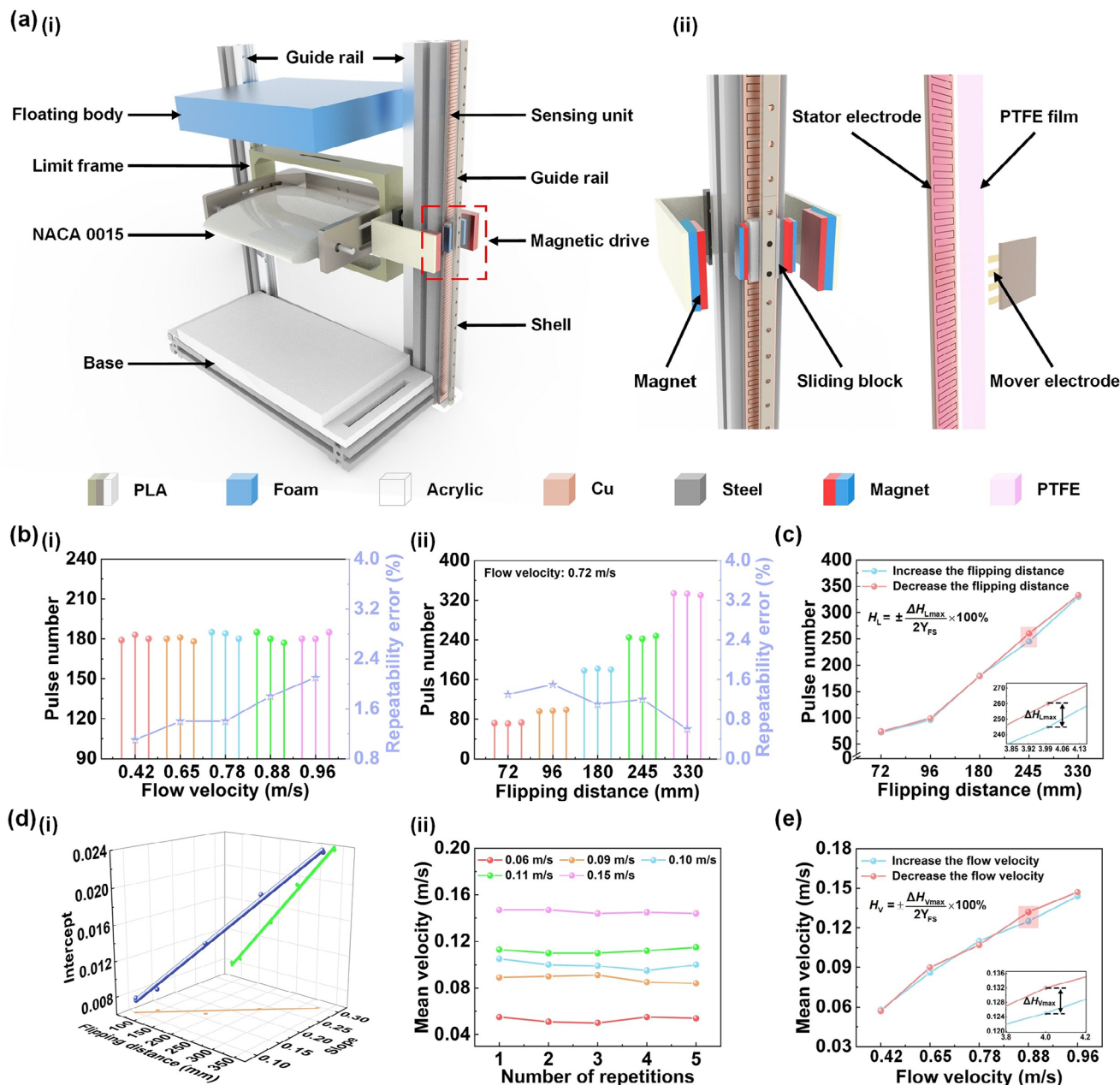


Figure 5. Sensing characteristics of FW-TENG under simulated water flow: a) Prototype structure diagram; b) (i) The pulse number and repeatability error at the same water level under different flow velocity, (ii) the pulse number and repeatability error at different water levels under the same flow velocity; c) Hysteresis of the water level sensing; d) (i) 3D linear fitting curves of flipping distance, slope, and intercept, (ii) reliability test of mean velocity; e) Hysteresis of the flow velocity sensing.

between the slider and the guide rail in FW-TENG, and the relative displacement between the magnet and other moving parts are important causes of hysteresis. At the same time, the eddy currents and turbulent pulsations formed around FW-TENG have temporal and spatial randomness, which will produce unstable forces on the movement of FW-TENG, further exacerbating the generation of hysteresis.

In addition, in order to confirm the relationship between flapping wing motion and water level and velocity, FW-TENG is studied deeply under different water levels and velocities, and

the characteristic information of flapping distance and flapping wing average velocity is extracted and analyzed. The specific analysis process is shown in Figure S9 (Supporting Information). First, the relationship between different flow velocities and flapping wing average velocities at different water levels is analyzed. As shown in Figure S10 (Supporting Information), the relationship between flow velocity and average velocity at the flapping distance of 180 mm is linear, and the correlation coefficient is 0.99. Subsequently, the relationship between flow velocity and average velocity at different flapping distances is linear, and

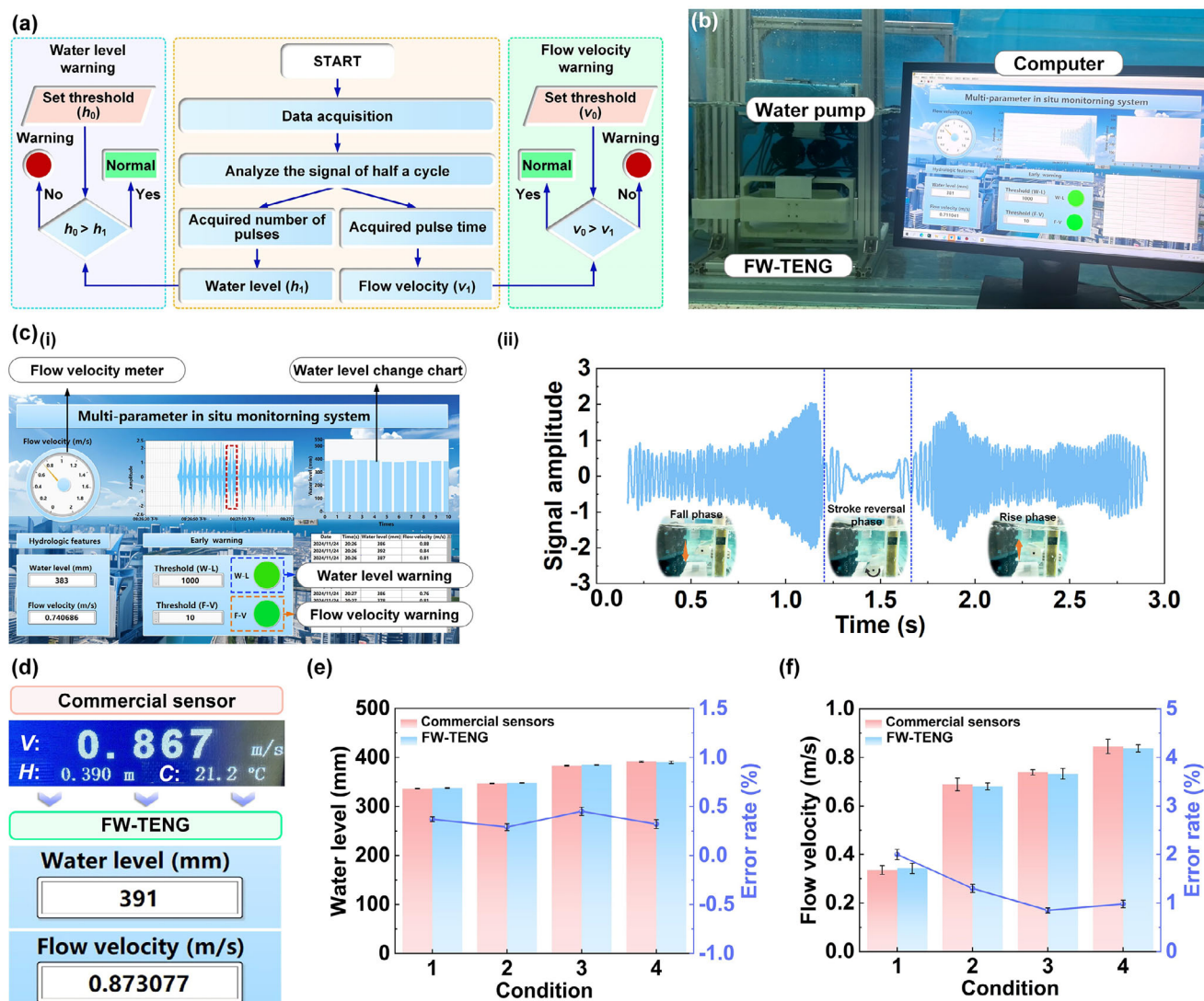


Figure 6. Application of FW-TENG in water level and flow velocity monitoring: a) Workflow diagram of integrated monitoring system; b) Application photograph of water level and flow velocity monitoring; c) On-line real-time monitoring process and monitoring signal amplification diagram; d) Comparison with commercial sensors; e, f) Comparison and error rate with commercial sensors at different water levels and flow velocity.

multiple slopes and intercepts are obtained from multiple linear relationships. Then, the relationship between flapping distance and slope and intercept is analyzed, as shown in Figure S11 (Supporting Information). Based on various linear relationships in this process, a 3D fitting curve with good linear relationships is finally obtained, as shown in Figure 5d(i). Next, the average velocity variation of FW-TENG at different flow velocities is measured for 5 consecutive times, as shown in Figure 5d(ii). The results show that FW-TENG has good stability and reliability. The hysteresis characteristics of flow rate monitoring are further analyzed, as shown in Figure 5e. The hysteresis error rate is less than 3.3% under different flow velocities, which means that it has high measurement accuracy and stability under different flow velocity conditions, and is suitable for long-term hydrological monitoring.

3. Application of Integrated Monitoring and Early Warning System

Combined with the LabVIEW data acquisition program, the integrated monitoring and early warning system is developed, and its program logic is shown in Figure 6a. The signals generated in the rising and falling phases of the FW-TENG were collected by an electrometer and a data acquisition card. The pulse number and its time of occurrence were then recorded by the LabVIEW program, and the flipping distance was calculated by multiplying the pulse number by the resolution. The water level information is finally obtained and displayed through real-time calculation of the flipping distance, and the calculation of the flow velocity is obtained based on a linear relation formula among the flipping distance, the mean velocity of the flapping wings, and the flow

velocity. Movies S3 and S4 (Supporting Information) illustrate the implementation of water level and flow velocity monitoring applications, respectively. Real-time warning can be achieved by setting water level and flow velocity thresholds as shown in Movie S5 (Supporting Information). In addition, the data is updated in real-time due to the movement of the continuous flapping wings, and historical data is recorded and analyzed to analyze the hydrology of the waters. The flow simulation system (Figure 6b) constructed during the application test consists of a flow pump, FW-TENG, and a computer. In addition, the water level and velocity are calibrated using a commercial Doppler velocimeter. Figure 6c(i) is an application display interface based on LabVIEW. Figure 6c(ii) shows the output signal of FW-TENG under one cycle and the corresponding motion state in actual water flow, where there is no electrical signal output in the stroke reversal phase. As shown in Figure 6d, the water level and flow velocity information monitored by the FW-TENG is very close to the values displayed on the commercial Doppler velocimeter. The variation of error rate of FW-TENG at different water levels and flow velocities is investigated in comparison with a commercial sensor, as shown in Figure 6e,f. The experimental results show that the maximum error rates of water level and velocity respectively, are less than 0.45% and 2%, which proves that FW-TENG has significant advantages in accuracy and reliability. FW-TENG is expected to play a more important role in the fields of intelligent water conservancy systems, ecological monitoring, and sustainable development.

4. Conclusion

In summary, a dual-function in situ monitoring method for water level and flow velocity is proposed, and a TENG based on a flapping wing structure is developed. First, the shape of the flapping wing is studied by fluid simulation. The simulation results show that the NACA 0015 flapping wing has the best starting moment and motion stability. On this basis, through the optimization design of the magnetic drive, the motion of the flapping wing is accurately transmitted to the TENG unit, and the transmission accuracy of displacement and velocity is 100% and 98%, respectively. A temperature and humidity test is carried out on the sealed sensing unit. The experimental results show that the sensing accuracy and signal amplitude of the sensing unit are not easily affected by temperature and humidity, and the validity of sensing data can be maintained. Furthermore, the sensing performance of FW-TENG is experimentally investigated under different water levels and flow velocities. The experimental results show that FW-TENG has good linearity, repeatability, and hysteresis characteristics, in which a resolution of water level is 1 mm. Finally, a dual-function monitoring and early warning system based on FW-TENG is developed. The system can monitor and record the flow velocity and water level in real-time, and the water level and flow velocity for early warning. Compared with a commercial Doppler sensor, the maximum water level and flow velocity error rate of FW-TENG are less than 0.45% and 2%, respectively. The above study shows that FW-TENG has potential applications in intelligent hydrological monitoring and can be widely used in agricultural irrigation, environmental monitoring, hydrological survey, and other fields.

5. Experimental Section

Fabrication of the FW-TENG: FW-TENG consists of a NACA 0015 flapping wing, floating body, slider, guide rail, sensing unit, magnetic drive, base, and limit frame, and the sensing unit was composed of a mover and stator. The electrode parts of the rotor and stator were composed of a printed circuit board (PCB) board and copper electrodes. The length of the stator PCB board was 540.0 mm, the width was 50.0 mm, and the thickness was 1.5 mm. The PCB board was covered with copper electrodes with a thickness of 35.0 μm , which were divided into left and right phases. A PTFE film 80.0 μm thick was adhered to the copper electrode. The length of the mover PCB board was 25.0 mm, the width was 50.0 mm, and the thickness was 1.5 mm, and the copper electrode with the same thickness was covered. The mover PCB board was stuck on the magnetic connection block fixed on the slider and placed on the guide rail to form the sensing unit. NACA 0015 flapping wing, base plate, and limit plate are all 3D printed with white resin. The NACA 0015 flapping wing had a chord length of 200.0 mm and a span length of 200.0 mm. The base was connected and fixed on the aluminum profile underwater through bolts. The floating body was made of foam material, and the sliding blocks fixed on both sides of the floating body were matched with the guide rails to float on the water surface.

Experimental Process and Measuring Equipment: A linear motion system (60ST-CJ101330L5-B, FGWISDOM) composed of a linear motor and a touch-screen controller was used to test the basic performance of TENG unit and optimize the design of the magnetic drive structure. Output performance (V_{OC} , I_{SC} , and Q_{SC}) was measured using a programmable electrometer (6514, Keithley) and a data acquisition (DAQ) card (USB-6218, NI), and measurement data were acquired using LabVIEW software. Then, in the process of the temperature and humidity experiment, the sensing unit was sealed and put into a constant temperature and humidity box (Y-HF-960L, Yuhang Zhida) for testing. Finally, in order to simulate the real flow scene, 4 \times 4 water pumps (EOW-22 M, Jecod) were used to simulate the flow environment and realize the control and adjustment of flow velocity. The water level was regulated by pumping water with a pump (SUB8500, MEDAS). The commercial Doppler hydrometer (HD-DP801, HORDE) was selected to calibrate the water level and velocity, and the measurement error was compared with that of FW-TENG.

Supporting Information

Supporting Information is available from the Wiley Online Library or from the author.

Acknowledgements

X.W., H.L., and J.Z. contributed equally to this work. The authors are grateful for the support from the China Postdoctoral Science Foundation (No. 2024M763218), and Beijing Natural Science Foundation (No. 3244038).

Conflict of Interest

The authors declare no conflict of interest.

Data Availability Statement

The data that support the findings of this study are available from the corresponding author upon reasonable request.

Keywords

dual-function, flapping-wing, in situ monitoring, triboelectric nanogenerator, water level-flow velocity method

Received: March 7, 2025

Revised: May 23, 2025

Published online:

- [1] M. van Vliet, J. Thorslund, M. Strokhal, N. Hofstra, M. Flörke, H. E. Macedo, A. Nkwasa, T. Tang, S. Kaushal, R. Kumar, A. van Griensven, L. Bouwman, L. M. Mosley, *Nat. Rev. Earth Environ.* **2023**, *4*, 687.
- [2] N. Njue, J. Stenfert Kroese, J. Graf, S. Jacobs, B. Weeser, L. Breuer, M. Rufino, *Sci. Total Environ.* **2019**, *693*, 133531.
- [3] A. Lay-Ekuakille, M. Ugwiri, V. Telesca, R. Velazquez, G. Passarella, S. Maggi, *Flow Meas. Instrum.* **2021**, *81*, 102042.
- [4] F. Alimenti, S. Bonafoni, E. Gallo, V. Palazzi, R. Vincenti Gatti, P. Mezzanotte, L. Roselli, D. Zito, S. Barbetta, C. Corradini, D. Termini, T. Moramarco, *IEEE Trans. Geosci. Electron.* **2020**, *58*, 5195.
- [5] M. Engram, F. Meyer, D. Brown, S. Clement, A. Bondurant, K. Spellman, L. Oxtoby, C. Arp, *Remote Sens. Environ.* **2024**, *305*, 114096.
- [6] H. Ji, S. Yoo, B.-J. Lee, D. Koo, J.-H. Kang, *Water* **2020**, *12*, 1771.
- [7] M. Durand, C. Dai, J. Moortgat, B. Yadav, R. Frasson, Z. Li, K. Wadkwoski, I. Howat, T. Pavelsky, *Remote Sens. Environ.* **2024**, *315*, 114455.
- [8] G. Dou, R. Chen, C. Han, Z. Liu, J. Liu, *Water* **2022**, *14*, 1890.
- [9] L. Andrews, T. E. Grantham, *Nat. Sustain.* **2024**, *7*, 714.
- [10] F. He, C. Zarfl, K. Tockner, J. Olden, Z. Campos, F. Muniz, J.-C. Svenning, S. Jähnig, *Nat. Rev. Earth Environ.* **2024**, *5*, 755.
- [11] F.-R. Fan, Z.-Q. Tian, Z. L. Wang, *Nano Energy* **2012**, *1*, 328.
- [12] Y. Yu, Q. Gao, X. Zhang, D. Zhao, X. Xia, J. Wang, H. Li, Z. L. Wang, T. Cheng, *Energy Environ. Sci.* **2023**, *16*, 3932.
- [13] Z. L. Wang, *Mater. Today* **2017**, *20*, 74.
- [14] C. Zhang, W. Tang, C. Han, F. Fan, Z. L. Wang, *Adv. Mater.* **2014**, *26*, 3580.
- [15] Z.-Q. Lu, L. Zhao, H.-L. Fu, E. Yeatman, H. Ding, L.-Q. Chen, *Nat. Commun.* **2024**, *15*, 6513.
- [16] Z. Liu, Y. Hu, X. Qu, Y. Liu, S. Cheng, Z. Zhang, Y. Shan, R. Luo, S. Weng, H. Li, H. Niu, M. Gu, Y. Yao, B. Shi, N. Wang, W. Hua, Z. Li, Z. L. Wang, *Nat. Commun.* **2024**, *15*, 507.
- [17] F. Dong, M. Zhu, Y. Wang, Z. Chen, Y. Dai, Z. Xi, T. Du, M. Xu, *Nano Energy* **2025**, *134*, 110550.
- [18] Q. Wang, D. Hu, X. Huang, Z. Chen, Z. Yuan, L. Zhong, Q. Sun, F. Wang, S. Xu, S. Chen, *Adv. Energy Mater.* **2024**, 2403931.
- [19] L. Liu, X. Zhao, T. Hu, F. Liang, B. Guo, K. Tao, *Nano Energy* **2024**, *132*, 110301.
- [20] C. Wang, Y. Yang, X. Zhang, P. Wang, X. Bi, H. Li, Z. L. Wang, T. Cheng, *Adv. Mater.* **2024**, *24*, 2410471.
- [21] Y. Yu, H. Li, X. Zhang, Q. Gao, B. Yang, Z. L. Wang, T. Cheng, *Joule* **2024**, *8*, 1855.
- [22] S. Panda, S. Hajra, Y. Oh, W. Oh, J. Lee, H. Shin, V. Vivekananthan, Y. Yang, Y. Mishra, H. Kim, *Small* **2023**, *19*, 2300847.
- [23] A. Barua, M. S. Rasel, *Sustain. Energy Technol. Assess.* **2024**, *61*, 103599.
- [24] K. Xue, C. Shao, J. Yu, H. Zhang, B. Wang, W. Ren, Y. Cheng, Z. Jin, F. Zhang, Z. Wang, R. Sun, *Adv. Funct. Mater.* **2023**, *33*, 2305879.
- [25] S. He, Z. Yang, J. Wang, X. Wang, J. Zhang, X. Guo, H. Li, T. Cheng, Z. L. Wang, X. Cheng, *Adv. Funct. Mater.* **2025**, *35*, 2415534.
- [26] W. Ma, P. Wang, B. Zhang, X. Li, Y. Gao, Z. Zhao, D. Liu, C. Li, J. Wang, *Adv. Energy Mater.* **2024**, *14*, 2304331.
- [27] D. Liu, C. Li, P. Chen, X. Zhao, W. Tang, Z. L. Wang, *Adv. Energy Mater.* **2023**, *13*, 2202691.
- [28] J. Shen, Z. Yang, Y. Yang, B. Yang, Y. Song, X. Cheng, Z. Lai, H. Zhao, L. Ji, Z. Zhu, J. Cheng, *Nano Energy* **2025**, *133*, 110453.
- [29] Y. Hu, Y. Hu, J. Li, Z. Wang, J. Ma, T. Cheng, J. Wen, *Mech. Syst. Signal Proc.* **2023**, *201*, 110649.
- [30] J. Mu, J. Song, X. Han, S. Xian, X. Hou, J. He, X. Chou, *Adv. Mater. Technol.* **2022**, *7*, 2101481.
- [31] J. Zhang, Y. Yu, H. Li, M. Zhu, S. Zhang, C. Gu, L. Jiang, Z. L. Wang, J. Zhu, T. Cheng, *Appl. Energy* **2024**, *357*, 122512.
- [32] M. N. Mumtaz Qadri, F. Zhao, H. Tang, *Int. J. Mech. Sci.* **2020**, *177*, 105587.
- [33] F. Zhao, M. N. Mumtaz Qadri, Z. Wang, H. Tang, *Int. J. Mech. Sci.* **2021**, *197*, 106323.
- [34] F. Zhao, Q. Jiang, Z. Wang, M. N. M. Qadri, L. Li, H. Tang, *Energy* **2023**, *268*, 126714.
- [35] L. Dong, J. Zhu, H. Li, J. Zhang, D. Zhao, Z. L. Wang, L. Gu, T. Cheng, *Nano Energy* **2024**, *127*, 109783.
- [36] S. Le Fouest, K. Mulleners, *Nat. Commun.* **2024**, *15*, 2770.
- [37] Y. Pan, S. Guo, J. Whidborne, X. Huang, *Aerosp. Sci. Technol.* **2024**, *148*, 109090.
- [38] M. Egerer, A. Ristolainen, L. Piho, L. Vihman, M. Kruusmaa, *IEEE Sens. J.* **2024**, *24*, 5986.
- [39] T. Li, C. Li, K. Wang, J. Wang, X. Wang, M. Li, F. Zhao, Y. Yao, *ACS Appl. Mater. Interfaces* **2024**, *16*, 33347.
- [40] Z. Chen, T. Wang, C. Zhao, Z. He, *Remote Sens.* **2023**, *15*, 4727.
- [41] T. Choo, G. Yun, H. Yoon, H. Noh, C. Bae, *Environ. Earth Sci.* **2016**, *75*, 115.
- [42] A. Affan, H. Nasir, T. Manzoor, A. Muhammad, *Comput. Electron. Agr.* **2022**, *198*, 107072.
- [43] P. Ma, Y. Wang, Y. Xie, Z. Huo, *Energy* **2018**, *155*, 1077.